Mon. Not. R. Astron. Soc. **000**, 000–000 (1994) Printed 17 June 1996

ASCA and ROSAT observations of the QSF3 field: the X-ray background in the 0.1–7 keV band

L.-W. Chen,[1] A. C. Fabian[1] and K. C. Gendreau[2]

[1] *Institute of Astronomy, Madingley Road, Cambridge CB3 0HA*

[2] *NASA/Goddard Space Flight Center, Greenbelt, MD 20771 U.S.A.*

ABSTRACT

The X-ray background from 0.1 to 10 keV has been studied using high spectral and spatial resolution data from the ASCA Solid-state Imaging Spectrometers (SIS) and ROSAT Position Sensitive Proportional Counter (PSPC). Analysing both the diffuse background radiation and resolved point sources, we have carried out a series of joint spectral fit of the ASCA and ROSAT data. As found previously with ASCA data alone, the spectrum of the X-ray background can be fit well by a single power-law from 1 to 7 keV; to account for the Galactic emission below 1 keV, a power-law plus two thermal component model fits well to the measurements of ASCA and ROSAT from 0.1 to 7 keV. Overall, the photon index of the power-law model ranges from 1.4 to 1.5, and no obvious excess is found between 1 and 3 keV as predicted from some previous observations. Below 1 keV, the models become more complicated and involve a mixture of extragalactic and Galactic sources. As some of the extragalactic contributions should be from point sources, we have examined the ASCA and ROSAT spectra of resolved sources individually: a stellar source having a well-fit thermal spectrum and two AGNs having a much steeper power-law spectrum (with photon index of about 3); the accumulated spectrum of other non-stellar sources resolved by ROSAT also has a steeper-than-average spectrum. This provides evidence that none of the resolved sources has a spectrum hard enough to match the X-ray background in a broad band. Fitting the X-ray background spectrum observed by ASCA and the accumulated point source spectrum by ROSAT together by varying the contribution from resolved point sources to the background, we find that the contribution is less than 30 per cent in the 0.5–2 keV band and drops to below 10 per cent in 2–10 keV. This fraction is provided by sources brighter than a few times 10^{-15} erg cm^{-2} s^{-1} (in the 0.5–2 keV band).

Key words: diffuse radiation – cosmology: observations – large-scale structure of Universe – X-rays: general

1. INTRODUCTION

The X-ray background (XRB) is the integrated emission of unresolved X-ray sources along the line of sight. The origin of the XRB is not yet clear and is mainly constrained by the observable spatial and spectral properties of the XRB (see Fabian and Barcons 1992 for a review). The homogeneity and isotropy of the XRB resulting from the surface number density and clustering of XRB point sources can be measured by imaging X-ray telescopes; spectral analysis of the XRB and resolved sources can provide additional information to identify the XRB origin. In other words, the integrated spectra of the assumed sources over redshift must reproduce the XRB, in terms of both spectral intensity and shape.

The 'spectral paradox' (Boldt 1987) is the common problem that most known X-ray sources have spectra which are too soft to account for the observed XRB and when their contribution to the XRB is removed the disparity increases. The XRB spectrum in the 3–50 keV band measured by HEAO-1 A2 (Marshall et al 1980) resembles a 40-keV bremsstrahlung spectrum and is equivalent to a power-law with photon spectral index Γ of 1.4 in the 3–10 keV band. Among X-ray sources in this energy band, Seyfert 1 galaxies have a $\Gamma = 1.7$ power-law spectrum in 2–20 keV (eg, Turner and Pounds 1989; Nandra 1991), and radio-loud and radio-quiet quasars have a $\Gamma = 1.66$ and $\Gamma = 2.0$ power-law spectrum in 2–20 keV (eg Williams et al 1992), respectively, all of which are steeper than the XRB spectrum. On the other hand, AGN spectra below 3 keV are steeper than those found at higher energies, the spectral slope of quasars is $\Gamma \sim 2.3 - 2.5$ according to the data obtained by ROSAT during the all sky survey (Schartel et al 1994). AGN may make a large contribution to the soft XRB because ROSAT observations have shown that the energy index of the best-fitting XRB power-law model can vary from 0.5 to 1.1 (Shanks et al 1991; Hasinger 1992; Wang & McCray 1993; Chen et al 1994; Georgantopoulos et al 1996);

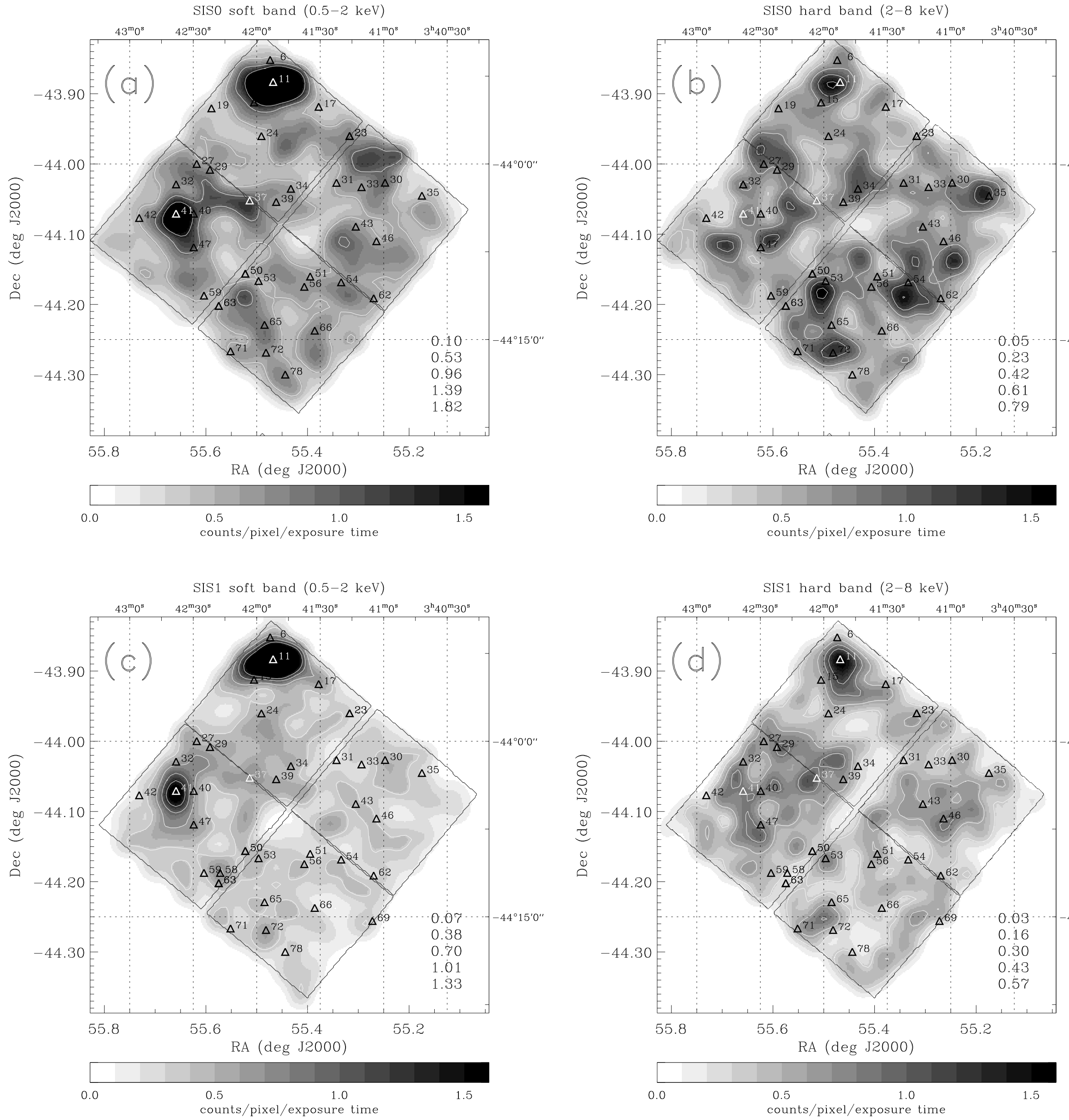

Figure. 1 (a) The ASCA SIS0 full field of view of the QSF3 field. The SIS is composed of four CCD chips (their outlines are shown by the dark solid lines). For SIS0 in (a)–(b), they are chip 3, 2, 1, 0 from top clockwise and chip 1, 0, 3, 2 for SIS1 in (c)–(d); each chip has an 11×11 arcmin^2 field of view. The pointing center is at RA (J2000) 55°.44, Dec (J2000) $-44°.12$. All the bad data have been screened except the particle background and the stray light. Each image has been binned into $\sim 30 \times 30$ arcsec^2 pixels and smoothed with a Gaussian filter of dispersion ~ 50 arcsec. The grey-scale bar is in unit of counts in the corresponding energy band per unit pixel per exposure time. The levels of the contours are the values at the lower-right conner of each image in the same unit of the grey-scale bar. (a) The QSF3 field in 0.5–2 keV, three bright point sources can be seen in the upper left quarter of this image (sources 11, 37, and 41, white triangles); other sources detected by the PSPC within the SIS field of view are indicated by black triangles (the sources are numbered according to the PSPC source list of Table 2a and Fig 2a). (b) The QSF3 field in 2–8 keV. The strong soft sources become much fainter. (c)–(d) Same as (a) and (b) but observed with SIS1. 10 sources are detected in the merged (SIS0+SIS1) soft SIS image and 6 in the hard image. See Table 2b and Sec 3.1.1 for details.

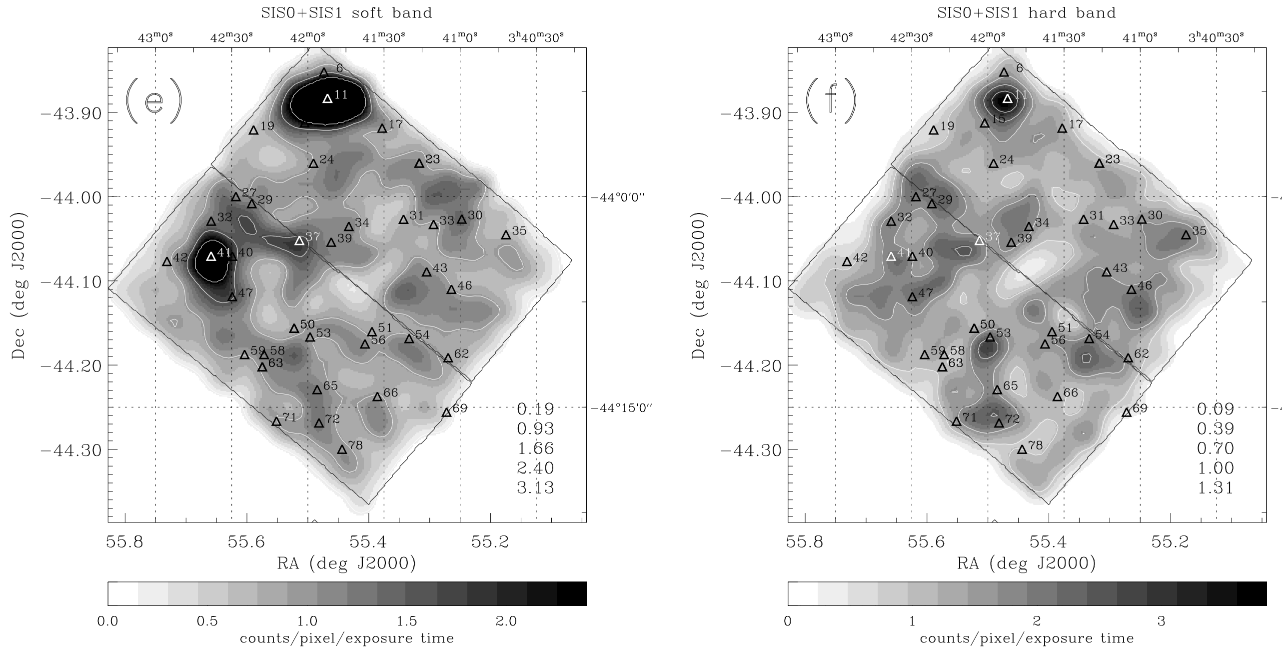

Figure. 1 (e)–(f) The merged ASCA SIS images in the soft (Fig. 1e) and hard band (Fig. 1f). The wider gap between 2 pairs of CCD chips disappears because of the offset along the SIS y-axis of the detector coordinate between the two SISs during the observation.

moreover, up to 70 per cent of the ROSAT XRB has been resolved and most sources are identified as AGN (Shanks et al 1991; Hasinger et al 1993). Unless either the XRB or AGN has a complicated spectrum, there is a problem to combine observations above and below 3 keV: the steeper AGN spectra would not have sufficient photons to fit the hard XRB on the one hand; on the other hand, the extrapolation from the hard XRB to the soft band would leave a soft excess. Therefore observations covering a broad bandpass are important and necessary to explore the origin of the XRB.

ASCA provides a chance to examine the XRB spectrum from at least 0.4 keV to 10 keV; recent ASCA observations (Gendreau et al 1995) find no evidence of a soft excess between 1–3 keV and show that the XRB spectral shape is well represented by a single power-law with $\Gamma = 1.4$ from 1 to 7 keV consistently. In this paper we use ASCA and ROSAT observations of the QSF3 field to investigate further the spectral properties of both the XRB and the resolved sources. The ASCA/ROSAT observations and data reduction are described in the next section, followed by the results of the ASCA/ROSAT spectral fitting. Implications for the origin of the XRB from our results are discussed in the fourth section and the conclusions.

2. ASCA/ROSAT OBSERVATIONS AND DATA REDUCTION

2.1 Observation

The QSF3 field is located in the Southern Sky centered at RA (J2000)= $03^{\rm h}41^{\rm m}45^{\rm s}$, Dec (J2000)= $-44^\circ07'08''$ [$(l,b) = 250^\circ.86, -51^\circ.99$), which is the pointing center of the ASCA observation used in this work]. Since it has a high Galactic latitude, the Galactic absorption is low, with an HI column density of 1.66×10^{20} cm^{-2} (derived from the radio observation by Heiles and Cleary, 1979).

The QSF3 field was observed to search for UV excess quasars and the later ROSAT observation (Shanks et al 1991) resolved ~ 30 per cent of the XRB into point sources above the flux of 10^{-14} erg cm^{-2} s^{-1}. Afterwards, 4 ASCA observations were carried out and there was another ROSAT observation during the period of ASCA observations.

2.1.1 ASCA Observation

ASCA was launched on 1993 Feb 20 (Tanaka et al 1994) and carries 2 Solid-state Imaging Spectrometers (SIS) and 2 Gas Imaging Spectrometers (GIS) with 4 identical X-Ray Telescopes (XRT; Serlemitsos et al 1995). It observed the QSF3 field four times during the period of Performance Verification (PV) when flight calibrations were carried out (Table 1a). The first observation was in July 1993, and the remaining three observations were in September 1993. Because the clean data of the last three SIS observations have exposure times less than 10 ks and one data set may have been damaged by telemetry saturation, we concentrate only on the first observation by the ASCA SIS, which has the best quality for our work.

2.1.2 ROSAT Observation

Two pointing observations of the same field by the ROSAT Position Sensitive Proportional Counter (PSPC) carried out in 1990 and 1993 are also used, of which the earlier and shorter observation with PSPCC has been used in Shanks et al (1991). The pointing centers of ROSAT observations

Table 1 (a) ASCA/ROSAT observations of the QSF3 field

Instrument	Dates	Pointing Centre RA, Dec (J2000)	Detector	Time*
ASCA	93-Jul-11/12	$55°.44, -44°.12$	SIS0	21303
			SIS1	17317
ROSAT	90-Jul-23/24	$55°.56, -44°.13$	PSPCC	21935
	93-Aug-04/05	$55°.55, -44°.13$	PSPCB	34735

* Exposure time is in seconds and calculated after screening described in Sec. 2.

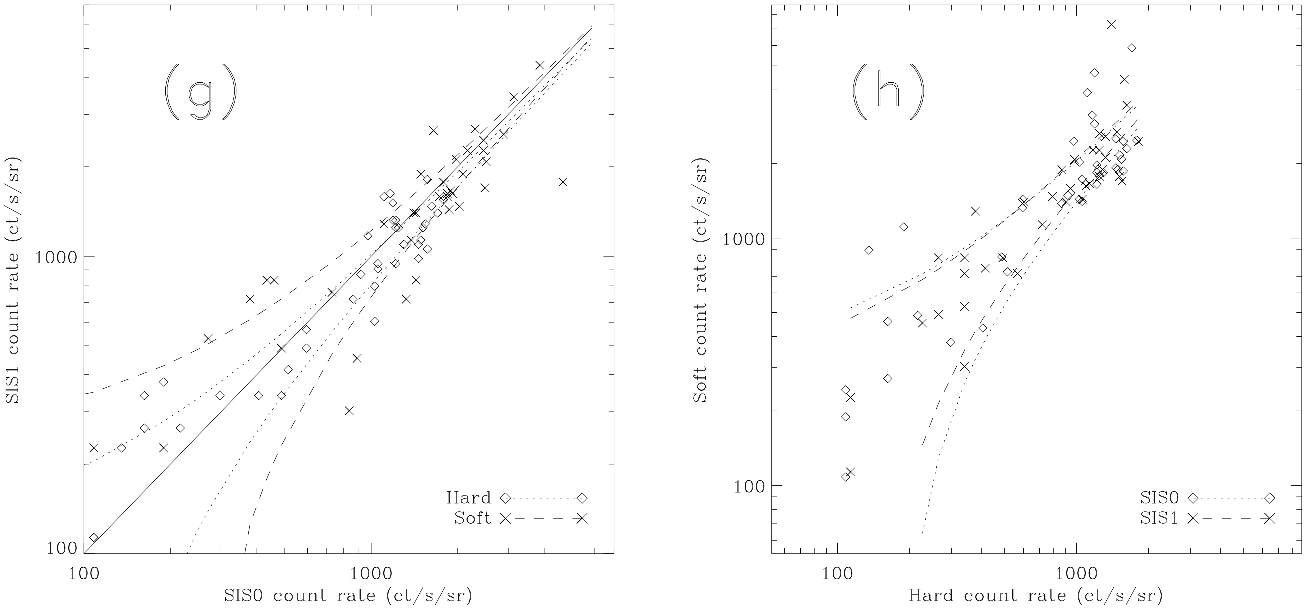

Figure. 1 (g)–(h) The pixel-to-pixel comparison of SIS0 and SIS1 image count rates in the hard (◇) and soft (×) band. The unit pixel size of images is about $4'15'' \times 4'15''$. Each data set is fit by a linear equation $y = Ax + B$ (x for the SIS0 count rate and y for the SIS1). The dotted and dashed lines are the 1σ interval of the best-fit in the hard and soft band, respectively. The solid line is for $y = x$. Fig 1h shows the soft SIS count rate against the hard SIS count rate (◇ for SIS0 and × for SIS1). Note that the bright pixels have the soft excess. The dotted and dashed lines are the 1σ interval of the best-fits.

Table 1 (b) Modes and screening criteria of ASCA observations (see Sec 2.2.1 for description)

Mode/HK Parameter	**Setting**	**Reference***
Clock Mode	4CCD	5.4.1
Data Mode	faint, bright	5.4.2
Grade	0, 2, 3, 4	5.4.4
Bit-rate	high, medium	2.2
`SAA`	0	5.2.2
`T_SAA`	>60 s	5.2.2
`COR_MIN`	>8 GeV/c	5.2.4
`T_DY_NT`	>200 s	5.2.4
`ELV_MIN`	>5 deg	5.2.5
`BR_EARTH`	>20 deg	5.2.5

*Section of the ABC Guide.

with PSPCC/B are at RA (J2000)= $03^{\mathrm{h}}42^{\mathrm{m}}24^{\mathrm{s}}/03^{\mathrm{h}}42^{\mathrm{m}}14^{\mathrm{s}}$, Dec (J2000)= $-44°07'48''$, so the most sensitive area of the PSPC just covers the same sky observed by the ASCA SIS (see Fig. 2a). Other detailed information of these observations is listed in Table 1a. Grey-scale images of the QSF3 field obtained from the ASCA SIS and the ROSAT PSPC are shown in Figs. 1a–f and Fig. 2a, respectively.

2.2 Data modeling and screening

2.2.1 ASCA Data: The Diffuse Foreground

The raw ASCA data were processed by the standard software FTOOLS to convert the telemetry data to "modally split science files" (see Day et al 1994, denoted as the ABC Guide hereafter) and we use SISCLEAN to remove hot and flicker pixels of SIS CCD chips. During the QSF3 field observation, the bright and faint-modes were used with 4 CCDs, which means that the 4 CCD chips give the maximum field of view for SIS observations. Observed events are initially split into the different modes according to the telemetry rate, and it is possible to merge the modal split data after converting the faint mode to bright mode. Furthermore, SIS X-ray events are classified into eight grades (0–7) based on the charge distribution in a three-by-three CCD pixel block. For the best quality of data, at the time of writing, only

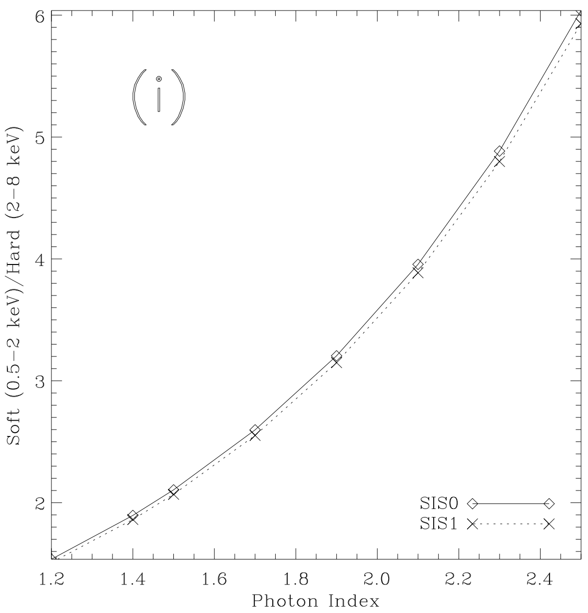

Figure. 1 (i) The soft/hard ratio as a function of the photon index of the power-law model plus the Galactic absorption toward the QSF3 field.

events with grades 0, 2, 3, and 4 are useful for analysing the bright mode data (eg up to 98 per cent of the particle background are associated with grade 7 events). Finally, events are accumulated into Pulse Invariant (PI) data, which are free from the chip-to-chip differences in gain and allow us to merge the counts from all 4 CCD chips into one spectrum.

The detected events are generally composed of vignetted counts, which are the read-out events of incoming photons originating from cosmic objects, and non-vignetted counts, which are induced by the instrument and have not been reflected by the telescope mirrors. The main non-vignetted component is the particle background which is dependent on the magnetic cut-off rigidity (Gendreau, 1995). This can be calibrated by using the data obtained when ASCA viewed the night earth.

Because the point spread function (PSF) of the XRT is very broad, we have used ray-tracing simulations to calibrate this energy-dependent broad PSF that will include counts from outside the nominal response range (the stray light); a special telescope response was made appropriate for the analysis of the XRB with the SIS data at the MIT Center for Space Research (Gendreau, 1995). Furthermore, the stray light contamination has particularly less affection to our field because there have no strong sources at least within 1 deg radius away from the SIS field of view according to the ROSAT image.

The vignetted counts contain astronomical information of interest (Galactic or extragalactic diffuse and discrete sources) as well as other foreground contaminations such as scattered solar X-rays. The contaminations are removed by filtering out their corresponding periods according to a set of housekeeping parameters recorded during observations as a time series function (see the ABC Guide). As a final check, we search for any extraordinary spike (more than 3σ above the mean value) appearing in the light curve of the diffuse background spectrum (resolved-source-free, see below) and reject data observed during these intervals.

Based on the housekeeping parameters, good data are collected when

1. the readout triggered by the South Atlantic Anomaly (SAA) particle flux is 0.
2. more than 1 min has passed since the SAA (T_SAA).
3. the magnetic cut-off rigidity (COT_MIN) exceeds 8 GeV/c.
4. more than 200 s has elapsed since the day/night transition (T_DY_NT).
5. the elevation angle (ELV_MIN, the target–satellite–dark earth angle) exceeds 5 deg, and the target–satellite–dark earth angle (BR_EARTH) exceeds 20 deg.

See Table 1b for a summary.

2.2.2 ASCA Data: The Discrete Source

Apart from using time filters, ray-tracing simulations, and night-earth data to remove the foreground diffuse contaminations, we have also excluded resolved sources from the SIS data for studying the nature of the extragalactic XRB.

Though the source detection ability of ASCA is limited by its intermediate spatial resolution, ROSAT observations and follow-up optical identifications can provide useful information on sources of flux down to 5×10^{-15} erg cm^{-2} s^{-1} in this region. Overlapping the sources catalog of the ROSAT observation, the 3 brightest PSPC sources (2 quasars and 1 Galactic star) are significantly detected (see Figs. 1–2), as well as some fainter PSPC sources above 2σ. Results and discussion of source detections are in Sec 3.1.

2.2.3 ASCA Data: SIS0/1 Consistency

To examine the consistency between the hard/soft SIS0/SIS1 images (eg Figs 1a–d), we have calculated pixel-to-pixel count rate correlations of hard SIS0–hard SIS1 (the diamonds in Fig 1g), soft SIS0–soft SIS1 (the crosses in Fig 1g), hard SIS0–soft SIS0 (the diamonds in Fig 1h), and hard SIS1–soft SIS1 (the crosses in Fig 1h). Each data point in Figs 1g–h indicates the count rate (count s^{-1} sr^{-1}) of the corresponding image with bin size $\approx 4'15'' \times 4'15''$. Using a robust least absolute deviation method, we fit each set of data points by a linear equation, $y = Ax + B$. For the SIS0–SIS1 correlation, we obtain the (SIS1 count)/(SIS0 count) ratios equal to 0.91 and 0.98 for the hard (2–8 keV) and soft (0.5–2 keV) band, respectively (with both best-fitting $B = 0$), showing that the two SIS observations are consistent with each other and that any visual fluctuations shown in the images are likely just due to the counting statistics. The error bar is derived from the mean absolute deviation of each data point to the best-fit in the y (ie the SIS1 count rate) direction. The 1σ uncertainty intervals are denoted by the dotted (2–8 keV) and solid (0.5–2 keV) lines in Fig 1g.

Fig 1h also shows the consistency of the hard–soft count correlations between SIS0 (the diamonds) and SIS1 (the crosses). The linear fitting described above has also been performed here, and we obtain $(A, B) = (1.86, 0.06)$ and (1.89,0.08) for SIS0 and SIS1, respectively. Pixels containing high count rates apparently have the soft excess, and their soft/hard ratio is above the average by a factor of a few. To translate the ratio to the power-law model, we simulate SIS spectra with various photon indices and calculate the soft/hard ratio of each case as shown in Fig. 1i.

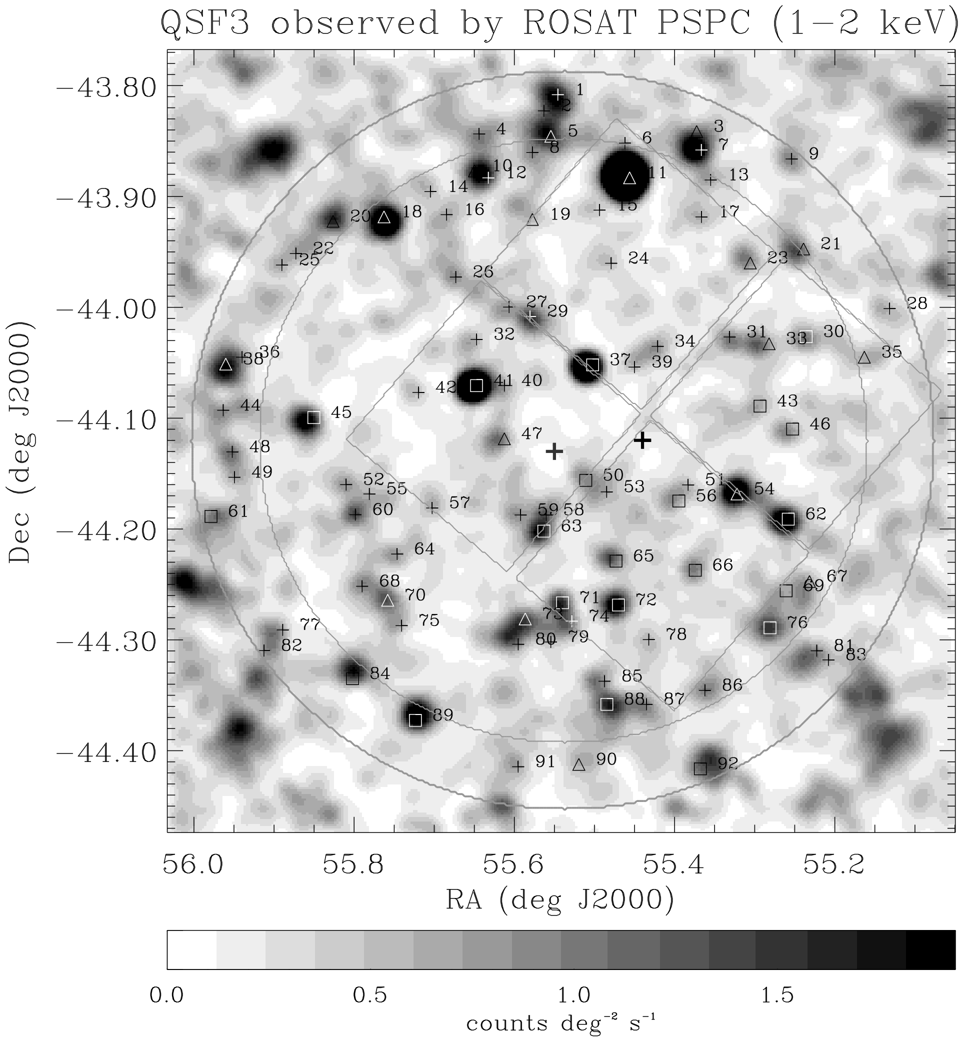

Figure. 2 (a) The merged ROSAT PSPCB+PSPCC central field of view of the QSF3 field with pixel size $\sim 15 \times 15$ arcsec^2 (exposure time ~ 57 ks). Only the central 16 arcmin region is used for our analysis (the inner circular line). The outer circular line indicates the region that was used in Shanks et al (1991), and the solid lines outline the field of view of the 4 SIS1 CCD chips. 92 sources are detected in this image and are numbered from north to south (also see Table 2a). Sources reported and identified as QSO/non-QSO by Shanks et al are represented by squares (□)/triangles (△), and the new detected sources by the crosses (+). The three brightest sources are sources 11, 41, and 37. The thick crosses in the center of the image are the pointing positions of the PSPC (the eastern one) and SIS (the western one) observations. The same image processing described in Fig. 1a has been applied on the image.

2.2.2 ROSAT Data

The ROSAT data are processed first by housekeeping parameter screening similar to that of the ASCA data, followed by calibrating the particle background (Snowden et al 1994; Plucinsky et al 1993) and excising sources. There are about 15 housekeeping parameters to monitor event quality (some of them are correlated) and our data selection criteria are based on the master veto count rate (EE_MV<170 count s^{-1}) and the accepted event rate (EE_AXE< 20 count s^{-1}) for both PSPCs, so that after the screening no temporal anomaly is shown in the light curves of these housekeeping parameters.

Using FTOOLS, we are able to merge the two ROSAT observations as well as their calibration files. Images and spectra are produced from the gain-corrected PI channel processed data. The exposure map correction has been done before merging images of two observations (Fig. 2a).

In the following analysis, the ROSAT data will be referred to as the merged data, and the two SIS data are always fit to a model simultaneously unless otherwise stated. All the ROSAT/ASCA spectra have been rebinned to at least 20 counts per channel so that χ^2 statistics can be applied.

3. SPECTRAL FITTING AND RESULTS

The XRB spectrum consists of extragalactic and Galactic diffuse emission as well as possible unresolved point sources.

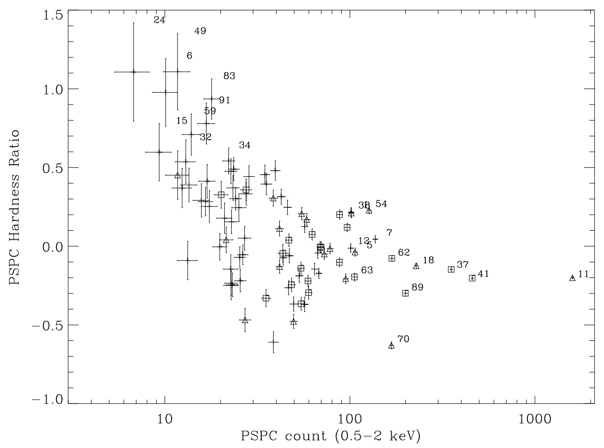

Figure. 2 (b) The hardness ratio of 92 sources detected by the PSPC in the 1–2 keV band (Table 2a). The symbol of each data point follows the same definition used in Fig 2. The error bar is reduced by a factor of 5 for display purposes. The hardness ratio is defined as $(H-S)/(H+S)$

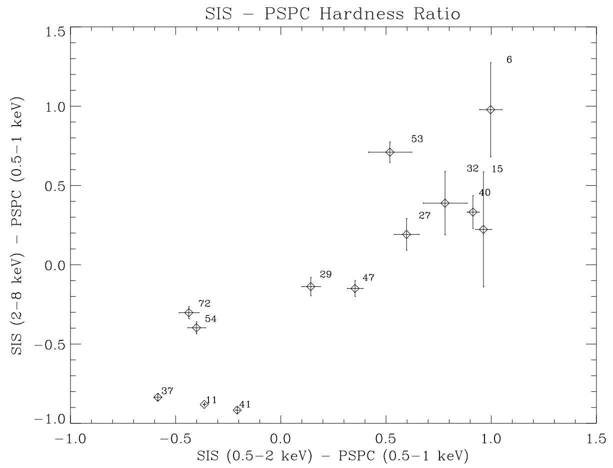

Figure. 2 (c) The cross SIS and PSPC hardness ratio of sources detected by SIS (see Table 2b). The error bar is reduced by a factor of 5.

Results from previous observations have modelled the Galactic XRB well as two Raymond-Smith hot plasma components (eg Hasinger 1992; Wang & McCray 1993; Chen et al 1994), where the soft one below 0.5 keV is from the local bubble and the hard one (roughly within 0.5–1 keV) is possibly from the Galactic halo (MODEL A hereafter). Contributions from point sources are believed to be dominated by AGN (including QSO), which has a power-law spectrum. MODEL A is hereafter referred to as the model of one power-law plus two Raymond-Smith components.

3.1 Spectral fitting of the resolved sources

What fraction of the XRB is from discrete sources is still not clear. Improvement of X-ray telescopes and detectors can help us to resolve the spatially featureless XRB into discrete sources, which could be part of the formally regarded XRB. Consequently, comparing the spatial and spectral characteristics of the resolved new sources with those of the XRB is one important and necessary stage to identify the real origin of the XRB.

3.1.1 Source detection: ROSAT data

As the ROSAT PSPC has better spatial resolution than the SIS, we use the following steps to detect point sources on the PSPC image first:

1 estimate the median of the whole image as the global background.
2 flag as the overdense region the pixels where the total count within a 0.5 and 1 arcmin radius region is 3σ higher than the global background.
3 repeat steps 1–2 excluding overdense regions to derive the second (and better estimated) median and overdense regions.
4 use a circular detection cell to scan over the overdense region and calculate the signal-to-noise ratio (SNR), where the noise is square root of the local background and the local background is the accumulated count of a concentric annulus region with the inner radius of 2 arcmin and the outer radius 3 arcmin while the overdense regions are avoided.
5 a source is detected when the SNR is over 3σ. The source position is determined by locating the local maximum position within a 0.75 arcmin radius region of the clustered 3σ pixels.

The basic pixel size of images during the search is 7.5 arcsec. 92 sources are detected within the inner 20 arcmin radius region of the PSPC (Table 2a), including all the sources reported by Shanks et al (1991). The three brightest sources include one Galactic star and two quasars at $z=0.64$ and 0.38 (sources 11, 37, and 41, and hereafter S1, Q1 and Q2, respectively).

3.1.2 Source detection: ASCA data

Applying the same technique on the merged 0.5–2 keV SIS0+SIS1 image, we have detected the three brightest PSPC sources along with 7 other 2σ sources, though some of them may be affected by the nearby bright sources (sources 6 and 15 by S1, source 40 by Q2). 6 sources are detected in the 2–8 keV band, including 3 sources which are not seen in the soft band (Table 2b). The detection cell is 1.5 arcmin, and the background is estimated from the global background instead of the local one.

3.1.3 Source hardness

The hardness ratio of the detected sources is also calculated and defined as $(H-S)/(H+S)$, where H is the hard band count (1–2 keV and 2–8 keV for the PSPC and SIS, respectively) and S is the soft count (0.5–1 keV and 0.5–2 keV for the PSPC and SIS, respectively). The counts of the source and background are extracted in the same way as described in the source detection procedures, except that for the SIS sources we use a 2-arcmin radius area. The results show no convincing evidence of strong dependence of the hardness ratio on the brightness of the PSPC sources (Fig. 2b).

The cross PSPC–SIS hardness ratio is calculated for the SIS sources. The PSPC soft band is taken as the soft band, and the SIS soft and the SIS hard counts are the hard count. Results are shown in Fig. 2c.

3.1.4 Spectral fitting

To produce spectra of resolved sources with enough counts for a meaningful spectral fitting, we only work on the

Table 2 (a) Sources detected by PSPC in 1–2 keV

No. (1)	RA	Dec (2)	Source Count (3)	Bkgd Count (4)	SNR (5)	Name (6)	Note (7)	Hardness Ratio (8)
1	55.55	−43.81	41.7± 8.0	3.6± 0.7	19.9		+	0.22 ± 0.14
2	55.56	−43.82	14.9± 4.5	6.0± 0.9	3.6		+	−0.15 ± 0.19
3	55.37	−43.84	26.4± 6.2	5.2± 0.8	9.2	XSF3:19	+	−0.05 ± 0.17
4	55.64	−43.84	18.2± 5.0	5.1± 0.9	5.7		+	−0.19 ± 0.21
5	55.55	−43.85	35.4± 6.8	5.7± 0.8	12.4	XSF3:17	+	−0.04 ± 0.13
6	55.46	−43.85	13.5± 4.1	5.4± 0.9	3.5		+ ⊙	0.98 ± 1.07
7	55.37	−43.86	58.2± 8.9	5.4± 0.8	22.8		+	0.04 ± 0.11
8	55.58	−43.86	17.5± 4.8	4.7± 0.8	5.9			0.41 ± 0.53
9	55.25	−43.87	20.9± 6.0	4.1± 0.7	8.2		+	−0.37 ± 0.23
10	55.65	−43.88	33.9± 6.8	7.2± 0.8	10.0	XSF3:20		−0.02 ± 0.16
11 (S1)	55.46	−43.88	488.8± 24.3	4.9± 0.6	218.3	XSF3:21	⊙	−0.20 ± 0.03
12	55.63	−43.88	43.0± 7.6	6.7± 0.8	14.0			−0.01 ± 0.14
13	55.35	−43.89	15.8± 4.6	4.0± 0.7	5.9		+	−0.37 ± 0.23
14	55.70	−43.90	12.4± 4.1	5.3± 0.8	3.1		+	−0.09 ± 0.61
15	55.49	−43.91	9.7± 3.4	4.1± 0.6	2.7		⊙	0.60 ± 0.91
16	55.68	−43.92	13.0± 4.1	5.6± 0.8	3.1			0.25 ± 0.50
17	55.37	−43.92	11.4± 3.8	3.6± 0.6	4.1		+	−0.07 ± 0.34
18	55.76	−43.92	67.1± 9.7	6.5± 0.8	23.7	XSF3:25	+	−0.12 ± 0.09
19	55.58	−43.92	11.0± 3.7	3.9± 0.6	3.6	XSF3:23		−0.48 ± 0.22
20	55.83	−43.92	30.0± 6.7	6.1± 0.9	9.6	XSF3:24	+	−0.21 ± 0.15
21	55.24	−43.95	24.6± 5.6	4.3± 0.6	9.8	XSF3:28	+	0.21 ± 0.20
22	55.87	−43.95	13.5± 4.8	5.4± 0.9	3.5		+	−0.61 ± 0.33
23	55.31	−43.96	20.8± 5.0	3.7± 0.6	8.9	XSF3:29	+	0.11 ± 0.24
24	55.48	−43.96	11.7± 3.7	4.0± 0.6	3.8			1.11 ± 1.56
25	55.89	−43.96	14.5± 5.1	4.7± 0.8	4.6		+	−0.25 ± 0.45
26	55.67	−43.97	17.6± 4.7	4.6± 0.6	6.0			0.37 ± 0.40
27	55.61	−44.00	18.9± 4.7	5.2± 0.7	6.0		⊙	0.15 ± 0.38
28	55.13	−44.00	16.6± 5.3	5.9± 0.8	4.4		+	−0.15 ± 0.46
29	55.58	−44.01	31.7± 6.1	5.0± 0.6	11.9		⊙	0.13 ± 0.18
30	55.24	−44.03	24.4± 5.3	3.6± 0.6	11.0	XSF3:32	+Q	−0.22 ± 0.18
31	55.33	−44.03	20.9± 4.9	5.0± 0.6	7.1			−0.07 ± 0.22
32	55.65	−44.03	16.3± 4.3	4.3± 0.7	5.7		⊙	0.54 ± 0.69
33	55.28	−44.03	21.0± 4.9	3.8± 0.6	8.9	XSF3:33	+	0.31 ± 0.25
34	55.42	−44.04	15.8± 4.2	4.4± 0.6	5.4			0.54 ± 0.41
35	55.16	−44.05	13.2± 4.2	4.5± 0.6	4.1	XSF3:35	+	0.04 ± 0.41
36	55.94	−44.05	21.1± 5.9	5.0± 0.7	7.3		+	0.48 ± 0.31
37 (Q1)	55.50	−44.05	152.2± 13.1	4.3± 0.6	71.6	XSF3:36	Q⊙	−0.15 ± 0.06
38	55.96	−44.05	35.2± 7.7	4.9± 0.8	13.7	XSF3:37	+	0.21 ± 0.15
39	55.45	−44.05	11.2± 3.5	3.1± 0.5	4.6			0.28 ± 0.45
40	55.61	−44.07	19.8± 4.5	3.8± 0.6	8.2		⊙	0.49 ± 0.36
41 (Q2)	55.65	−44.07	180.7± 13.9	5.0± 0.6	78.7	XSF3:38	Q⊙	−0.20 ± 0.05
42	55.72	−44.08	11.9± 3.6	3.4± 0.5	4.6			0.39 ± 0.53
43	55.29	−44.09	14.6± 4.1	4.2± 0.6	5.0	XSF3:42	Q	−0.33 ± 0.27
44	55.96	−44.09	16.6± 5.2	6.5± 0.9	4.0		+	0.25 ± 0.45
45	55.85	−44.10	45.3± 7.5	4.5± 0.6	19.3	XSF3:44	+Q	0.20 ± 0.15
46	55.25	−44.11	22.0± 5.0	4.1± 0.6	8.9	XSF3:45	+Q	−0.37 ± 0.20
47	55.61	−44.12	22.9± 5.0	4.6± 0.6	8.6	XSF3:46	⊙	−0.13 ± 0.22
48	55.95	−44.13	21.4± 5.9	5.0± 0.8	7.3		+	0.39 ± 0.34
49	55.95	−44.15	12.4± 4.7	4.3± 0.7	3.9		+	1.11 ± 1.20
50	55.51	−44.16	22.3± 5.0	3.5± 0.5	10.0	XSF3:48	Q	0.04 ± 0.20

three brightest sources with their PSPCC+PSPCB and SIS0+SIS1 spectra. The area size for creating the source spectrum is based on that the half power diameter of the ASCA XRT is 3 arcmin (the ABC Guide) and the full width half maximum of the ROSAT PSPC is about 25 arcsec within the inner 15 arcmin radius region (Hasinger et al 1995) as well as the brightness of the source and background.

We accumulate the PSPC source spectrum from a circular region of radius ~ 1.5 arcmin around the source position, and the background spectrum is produced from a concentric

Table 2 (a) – *continued*

No. (1)	RA	Dec (2)	Source Count (3)	Bkgd Count (4)	SNR (5)	Name (6)	Note (7)	Hardness Ratio (8)
51	55.38	−44.16	11.7± 3.7	5.0± 0.7	3.0			−0.25 ± 0.37
52	55.81	−44.16	17.5± 4.7	6.2± 0.7	4.5			−0.23 ± 0.39
53	55.48	−44.17	12.5± 3.8	5.2± 0.6	3.2		⊙	0.48 ± 0.39
54	55.32	−44.17	70.9± 9.0	4.5± 0.6	31.3	XSF3:51	⊙	0.23 ± 0.11
55	55.78	−44.17	14.2± 4.1	4.4± 0.6	4.7			−0.05 ± 0.31
56	55.39	−44.17	16.3± 4.4	4.3± 0.6	5.8	XSF3:53	Q	−0.25 ± 0.21
57	55.70	−44.18	13.1± 3.8	4.5± 0.6	4.0			0.37 ± 0.62
58	55.56	−44.19	26.5± 5.5	4.8± 0.6	9.8			−0.17 ± 0.16
59	55.59	−44.19	18.1± 4.5	5.4± 0.6	5.5			0.71 ± 0.66
60	55.80	−44.19	29.6± 6.1	5.8± 0.7	9.8			0.45 ± 0.30
61	55.98	−44.19	20.1± 6.1	6.0± 0.9	5.7	XSF3:56	+Q	−0.04 ± 0.28
62	55.26	−44.19	67.1± 8.8	4.0± 0.6	31.8	XSF3:54	+Q	−0.08 ± 0.09
63	55.56	−44.20	43.7± 7.1	4.6± 0.6	18.2	XSF3:57	Q	−0.20 ± 0.12
64	55.75	−44.22	19.5± 4.9	5.3± 0.7	6.2			0.29 ± 0.53
65	55.47	−44.23	28.9± 5.8	5.7± 0.7	9.8	XSF3:58	Q	−0.14 ± 0.19
66	55.37	−44.24	19.6± 4.8	4.6± 0.6	7.0	XSF3:59	Q	0.36 ± 0.34
67	55.23	−44.25	16.4± 4.4	8.0± 0.9	3.0	XSF3:63	+	0.45 ± 0.77
68	55.79	−44.25	17.4± 4.6	4.0± 0.6	6.7			0.44 ± 0.34
69	55.26	−44.26	11.7± 3.7	4.9± 0.7	3.1	XSF3:61	+Q	0.33 ± 0.43
70	55.76	−44.26	32.3± 6.2	4.9± 0.6	12.3	XSF3:64		−0.63 ± 0.11
71	55.54	−44.27	41.0± 6.9	3.7± 0.6	19.3	XSF3:65	Q	0.07 ± 0.17
72	55.47	−44.27	53.4± 8.0	5.0± 0.7	21.6	XSF3:66	Q⊙	0.12 ± 0.13
73	55.59	−44.28	30.6± 6.1	3.7± 0.6	14.0	XSF3:68		0.17 ± 0.19
74	55.53	−44.28	25.1± 5.5	3.9± 0.7	10.7			0.31 ± 0.24
75	55.74	−44.29	14.9± 4.3	4.3± 0.6	5.1			−0.22 ± 0.35
76	55.28	−44.29	34.5± 6.4	5.2± 0.7	12.8	XSF3:67	+Q	−0.10 ± 0.14
77	55.89	−44.29	15.1± 5.0	6.4± 0.9	3.5		+	0.18 ± 0.48
78	55.43	−44.30	12.3± 3.9	4.9± 0.7	3.3			−0.00 ± 0.42
79	55.55	−44.30	9.9± 3.5	2.6± 0.5	4.5			0.30 ± 0.36
80	55.60	−44.30	22.7± 5.4	4.7± 0.7	8.3			−0.04 ± 0.17
81	55.22	−44.31	17.6± 4.7	6.0± 0.9	4.7		+	0.25 ± 0.23
82	55.91	−44.31	13.6± 4.8	5.6± 0.8	3.4		+	0.05 ± 0.38
83	55.21	−44.32	11.9± 4.0	4.8± 0.8	3.3		+	0.94 ± 0.64
84	55.80	−44.33	25.9± 6.1	4.8± 0.7	9.6	XSF3:70	+Q	−0.00 ± 0.17
85	55.49	−44.34	21.9± 5.2	5.4± 0.7	7.1			−0.06 ± 0.22
86	55.36	−44.35	16.3± 4.5	4.6± 0.6	5.4		+	−0.26 ± 0.22
87	55.44	−44.36	20.0± 5.0	6.4± 0.8	5.3			0.33 ± 0.36
88	55.48	−44.36	31.1± 6.2	5.0± 0.7	11.6	XSF3:71	Q	−0.01 ± 0.17
89	55.72	−44.37	56.6± 9.1	4.1± 0.6	26.0	XSF3:72	+Q	−0.30 ± 0.10
90	55.52	−44.41	13.1± 4.1	4.9± 0.7	3.7	XSF3:78	+	−0.47 ± 0.37
91	55.60	−44.41	17.7± 4.9	4.0± 0.6	6.9		+	0.78 ± 0.65
92	55.37	−44.42	20.4± 5.5	5.8± 1.1	6.1	XSF3:77	+Q	−0.30 ± 0.21

(1) Sources numbered as shown in Figs 1–2. (2) Coordinates in J2000. (3) PSPCB+PSPCC source counts collected from a 0.75 arcmin radius region in 1–2 keV. (4) Background counts collected from a ring centred on the source with the inner radius 2 arcmin and the outer radius 3 arcmin, and normalised by the same area size as that of the source count. (5) Signal-to-noise ratio in 1–2 keV, the detection cell size is 0.75 arcmin radius. (6) Survey name used in Table 1 of Shanks et al (1991), sources newly found in this work are blank in this column. (7) Q: sources identified as QSO by Shanks et al (1991); ⊙: sources also detected by the ASCA SIS (Table 2b). '+' Sources located between the the inner 16 arcmin and the 20 arcmin radius region of the PSPC. Sources 11, 37, 41 are named as S1, Q1 and Q2, respectively in this work.

ring with the inner radius ~ 3 arcmin and the outer radius ~ 7 arcmin, where bright sources are removed from the ring.

For the ASCA data, we choose a larger area to collect source counts; it is an elliptic region (because of the SIS PSF) with a 4 arcmin semimajor axis and 3.5 arcmin semiminor axis for S1, a circle with the radius ~ 4 and 3 arcmin for Q2 and Q1, respectively. The background spectrum for these three sources is created from the blank region be-

Table 2 (b) Sources detected by ASCA SIS

No.	Count (soft)	Count (hard)	SNR (soft)	SNR (hard)
6	44.01± 7.64	5.66± 5.27	7.0	
11 (S1)	246.86± 11.99	33.59± 5.41	39.2	6.8
15	55.15± 6.93	1.63± 3.66	8.8	
27	22.14± 5.83	7.89± 5.49	3.5	
29	19.25± 5.71	10.45± 5.64	3.1	2.1
32	13.61± 5.25	3.78± 3.81	2.2	
37 (Q1)	30.06± 6.24	10.03± 4.34	4.8	2.0
40	73.12± 7.55	6.63± 3.98	11.6	
41 (Q2)	100.08± 8.40	6.63± 3.98	15.9	
47	27.19± 5.84	9.62± 4.17	4.3	
53	10.82± 5.49	19.44± 5.19		3.9
54	11.86± 5.39	11.68± 4.48		2.4
72	9.21± 5.01	12.62± 4.34		2.6

Sources detected above 2 σ on the merged SIS0+SIS1 images (exposure time $\sim$ 40 ks) in either 0.5–2 keV or 2–8 keV band. Source counts are accumulated from a 1.5 arcmin radius region (background counts are subtracted in this table); the background counts are estimated from the bright-source-free region of the whole image, which are 39.71 $\pm$ 0.84 and 24.33 $\pm$ 0.64 for the soft and hard band, respectively. We use a 1.5 arcmin radius detection cell to derive the significance of source detection (SNR).

tween S1 and Q1.

Fitting the 2 quasar spectra by a single power-law (with Galactic absorption) we found that their spectra are much steeper than that of the XRB. Fitting the PSPC and SIS data individually, we obtain similar results with good reduced chi-square χ^2_ν, the photon index Γ ranges from 3.0 to 3.7 for both Q1 and Q2. Fitting the ASCA/ROSAT data jointly, Γ is 3.08 $\pm$ 0.10 and $3.09^{+0.05}_{-0.07}$ (the denoted uncertainty refers to 90 per cent confidence interval through out this paper unless otherwise stated) for Q1 and Q2, respectively. The stellar spectrum is fit by a Raymond-Smith plasma emission model, with $kT = 0.81^{+0.05}_{-0.06}$ keV, abundance $Z = 0.05 \pm 0.01$ solar from the joint fitting. Although the abundance is low, an alternative thermal bremsstrahlung cannot have a good fit ($\chi^2_\nu > 2$), showing the data to be sensitive enough to distinguish these two models. The results of the separate and joint fitting are shown in Table 3a.

To study the spectral property of other fainter sources resolved by the ROSAT PSPC within the inner $\sim$ 16 arcmin region in general, especially AGN, we have added up all the spectrum of sources which have been identified as AGN (sources with a 'Q' in the 'Note' column of Table 3a) and fit them by a power-law. Not too surprisingly, the total spectrum has photon index $\Gamma = 2.76^{+0.07}_{-0.06}$ (χ^2_ν=1.1) which is softer than that of average AGN (see Figs. 8–9 for its folded model and spectrum); removing the two bright quasars (ie, Q1 and Q2) analysed above, we obtain the best-fit $\Gamma = 2.54 \pm 0.10$ (χ^2_ν=0.98). The integrated ROSAT-resolved AGN spectrum with/without Q1 and Q2 will be denoted as RS_QA/RS_QB hereafter.

3.2 Spectral fitting of the XRB with ASCA data

Since complications in the spectrum of the 0.1–10 keV cosmic background are only significant below 1 keV, we first fit the SIS data in the 1–7 keV band with a single power-law model, giving photon index $\Gamma = 1.44^{+0.08}_{-0.07}$ and normalization $A = 10.10^{+0.60}_{-0.60}$ keV cm^{-2} s^{-1} sr^{-1} keV^{-1}, with χ^2_ν=1.15. This result is consistent with recent work by Gendreau et al (1995). Dividing the spectrum into 1–3 and 3–7 keV and fitting by the same model, we have similar results (see Table 3b).

Extending the data down to 0.4 keV, an excess below 1 keV (mostly of Galactic origin) is clearly seen. Introducing a Raymond-Smith hot plasma model and the HI column density (fixed at 1.66 $\times$ 10^{20} cm^{-2}) to correct the Galactic absorption, we obtain an almost unchanged best fit of the power-law component, $\Gamma = 1.44^{+0.07}_{-0.06}$ and A = 10.2 keV

Table 3 (a). Best-fits of the resolved sources

Source		Flux a	Flux b	Flux c	Best-fit	χ^2_ν
S1 (star)	SIS+PSPC	27.9	75.0	8.8	$kT = 0.81^{+0.05}_{-0.06}$ keV, $0.05 \pm 0.01 Z_\odot$	1.50
					$kT_{\rm bremss} = 1.01$ keV	2.08
	SIS				$kT = 1.13^{+0.28}_{-0.18}$ keV, $0.09^{+0.19}_{-0.08} Z_\odot$	1.28
					$kT_{\rm bremss} = 1.05^{+0.34}_{-0.23}$ keV	1.39
	PSPC				$kT = 0.74^{+0.07}_{-0.05}$ keV, $0.05 \pm 0.01 Z_\odot$	1.39
					$kT_{\rm bremss} = 1.01$ keV	2.35
Q1 ($z = 0.64$ QSO)	SIS+PSPC	4.8	9.0	2.1	$\Gamma = 3.08 \pm 0.10$	1.18
	SIS				$\Gamma = 3.71^{+1.93}_{-1.73}$	1.44
	PSPC				$\Gamma = 3.06 \pm 0.10$	1.12
Q2 ($z = 0.38$ QSO)	SIS+PSPC	8.2	30.4	8.07	$\Gamma = 3.09^{+0.05}_{-0.07}$	1.28
	SIS				$\Gamma = 3.01^{+0.65}_{-0.63}$	1.22
	PSPC				$\Gamma = 3.23^{+0.16}_{-0.10}$	1.21
RS_QA	PSPC				$\Gamma = 2.76^{+0.07}_{-0.06}$	1.1
RS_QB	PSPC				$\Gamma = 2.54 \pm 0.10$	0.98

Flux is in unit of 10^{-14} erg cm^{-2} s^{-1}. a in the PSPC 0.5–2 keV band, b in the SIS 0.5–2 keV band, c in the SIS 2–10 keV band. S1 is fit by a Raymond-Smith gas (T) and thermal bremsstrahlung ($T_{\rm bremss}$) model; Q1 and Q2 are fit by a power-law. RS_QA and RS_QB are the accumulated ROSAT non-stellar spectra as defined at the end of Sec. 3.1.

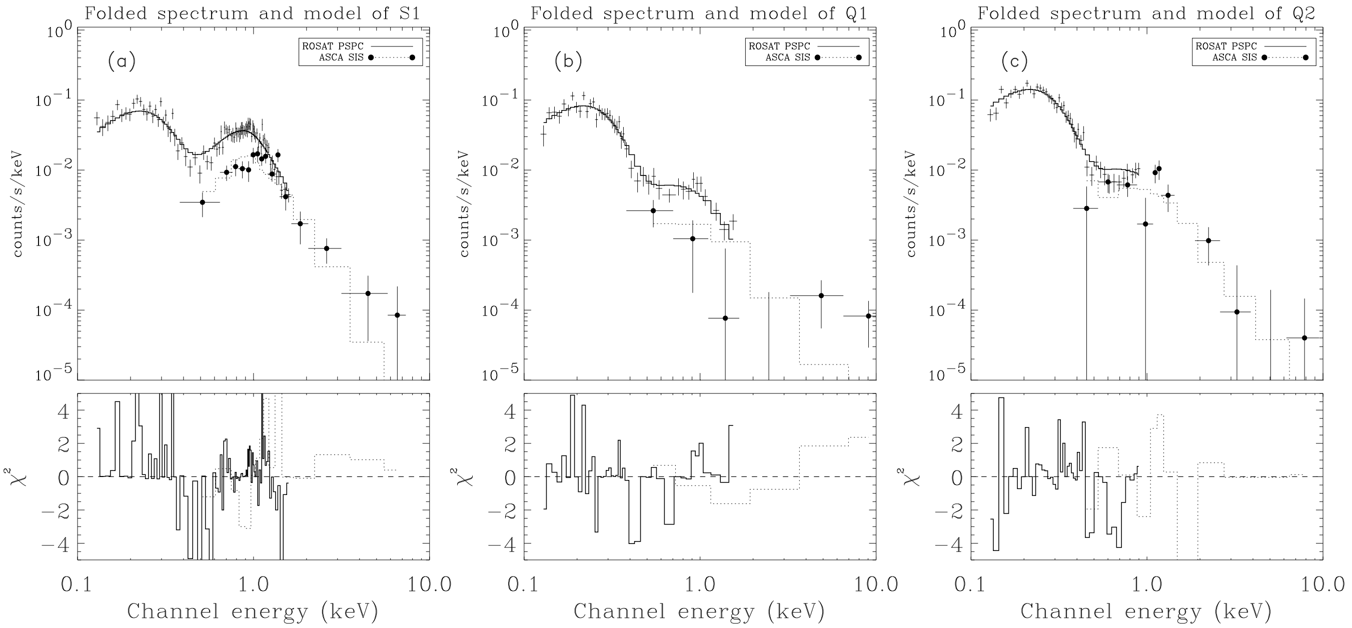

Figure. 3 Spectra of three sources resolved by the SIS. (a) Source S1: a star (b) Source Q1: a z=0.6 quasar (c) Source Q2: a z=0.3 quasar. In each figure, the count spectrum and folded model are shown in the upper panel and the χ^2 contributions to each bin in the bottom panel. The filled circles and dots represent the folded spectrum measured by the ASCA SIS and the ROSAT PSPC, respectively, and the dotted and solid lines are the respective best-fitting model. See Table 3a for the best-fitting results.

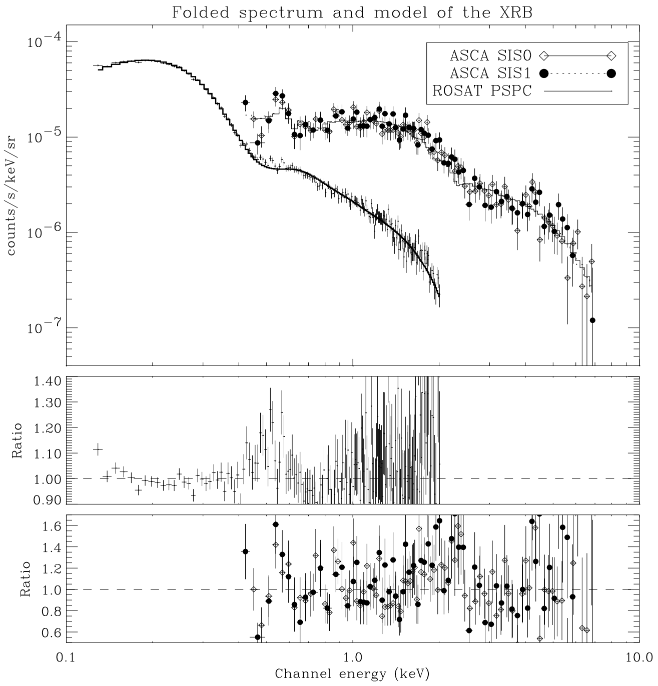

Figure. 4 Folded XRB model (MODEL A) and spectrum measured by the SIS (0.4–7 keV) and the PSPC (0.1–2 keV). Data divided by the best-fitting model are shown in the 2 panels at the bottom. Note that the amplitudes of the ROSAT spectrum and model have been reduced by a factor of 20.

cm^{-2} s^{-1} sr^{-1} keV^{-1}with χ^2_ν=1.24, while the hot gas has a temperature of 0.11 keV with a fixed solar abundance.

To include the contribution from the local bubble below 0.5 keV, we add one more soft hot plasma component (MODEL A) and obtain the temperature of the soft component $kT_{\rm s}$=0.04 keV and the hard one $kT_{\rm h}$=0.11 K while the power-law component remain unchanged. Replacing the soft hot plasma component with either a power-law or a bremsstrahlung component does not improve previous fits, and eventually there are probably only 1–2 binned channels below 0.5 keV to constrain the local bubble model. This implies that to consider the overall constraints on the 0.1–10 keV XRB model, it is helpful to have a joint fit with the ROSAT data to provide an extra constraint on the 0.1–2.0 keV band.

3.3 Spectral fitting of the XRB with ROSAT data

The ROSAT XRB spectrum is accumulated from events within the inner 16 arcmin radius region, covering a similar sky region to the SIS data (Fig. 2a). Only the 3 brightest point sources resolved by ASCA have been removed from the data so we can easily compare the result with its ASCA counterpart, though there are more other fainter sources detected in this region.

Fitting the ROSAT spectrum in the 1–2 keV band alone by a single power-law, we have Γ = $1.65^{+0.18}_{-0.17}$, A = $11.4^{+0.50}_{-0.60}$ keV cm^{-2} s^{-1} sr^{-1} keV^{-1} and χ^2_ν= 1.14. Using 0.1–2 keV to fit complicated models like MODEL A cannot have a reasonably good fit without further constraints or assumptions. On the other hand, to check how the faint sources of flux from 10^{-13} to 10^{-14} contribute to the XRB,

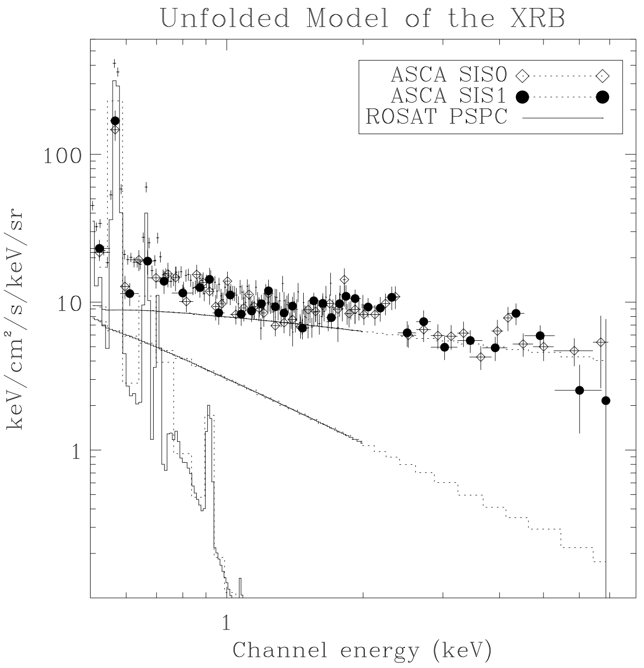

Figure. 5 Unfolded XRB spectrum above 0.5 keV measured by the SIS and the PSPC. The dotted and solid lines represent the best-fitting model components (MODEL B) of the ASCA and ROSAT data respectively. The model consists of three components to take into account contributions from Galactic emission (the lines with line features), AGN-like sources (the steep lines with photon index $\Gamma_{\rm src}$ fixed at 2.5) and the yet unknown XRB sources (the flat lines).

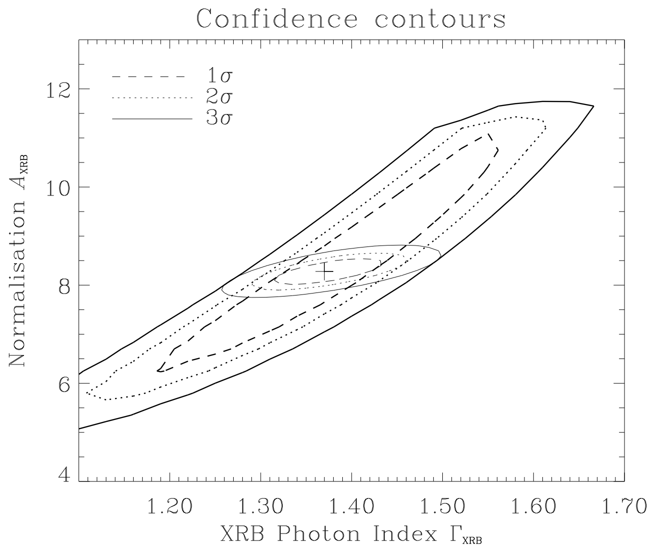

Figure. 6 Confidence contours of the XRB photon index and normalisation for the spectral fitting in Fig. 5. The cross is the best fit and the small contours are calculated by holding the steep power-law component fixed at $\Gamma_{\rm src} = 2.5$ and $A_{\rm src} = 3.16$.

we excise all the detected PSPC sources from the data (soft-AGN-free XRB, hereafter). The excised region is about 2 arcmin radius for the bright sources but smaller for other faint sources because outside the 0.75 arcmin radius their residual counts for most cases are negligible to the XRB. The best fit to the soft-AGN-free XRB in 1–2 keV is $\Gamma = 1.53$ and $A = 6.5$ keV cm^{-2} s^{-1} sr^{-1} keV^{-1}.

We note, in comparison to the ASCA result, the steeper result obtained from ROSAT has also been seen in other ASCA/ROSAT simultaneous fitting (eg Fabian et al 1994), it indicates that the discrepancy may be due to calibration uncertainties in ROSAT.

3.4 Joint fitting of the XRB with ASCA/ROSAT data

3.4.1 Single Power-law Model of the Extragalactic XRB

Joint spectral fitting of the ASCA/ROSAT data has been carried out by forcing each data set to have the same photon index for the power-law component and temperature of the thermal component. A simultaneous fit of the 1–7 keV ASCA and 1–2 keV ROSAT spectra by a single power-law gives $\Gamma = 1.4^{+0.14}_{-0.01}$ and the average normalization of 10.5 keV cm^{-2} s^{-1} sr^{-1} keV^{-1}, χ^2_ν= 1.15. Using the 1–3 keV ASCA data instead, we have $\Gamma = 1.44^{+0.11}_{-0.11}$ and the average normalization 10.5 keV cm^{-2} s^{-1} sr^{-1} keV^{-1}, χ^2_ν= 1.15

Fitting the 0.4–7 keV ASCA and 0.5–2 keV ROSAT spectra by a Galactic absorbed power-law and Raymond-Smith model, we obtain a slight softer power-law: $\Gamma = 1.47^{+0.07}_{-0.43}$ $A = 9.8$ keV cm^{-2} s^{-1} sr^{-1} keV^{-1}, $kT = 0.11$ keV with χ^2_ν=0.98. It is still not easy to determine the abundance of the halo gas, as it is not sensitive to the fitting (with a large error bar) though we have obtained its best fit 0.8 solar abundance, while other best-fitting values remain the same.

Finally, we use the total band of both data set, namely, 0.4–7 keV for the ASCA data and 0.1–2 keV for the ROSAT data, to constrain contributions from the Galactic halo, local bubble, and the extragalactic sources. Fitting data with MODEL A, we have $\Gamma = 1.44^{+0.06}_{-0.06}$, $A = 10.4$ keV cm^{-2} s^{-1} sr^{-1} keV^{-1}(on average), $kT_{\rm h}$= 0.12 keV, $kT_{\rm s}$= 0.05 keV, χ^2_ν=1.12. Using a thermal bremsstrahlung model for the soft thermal component, the best-fitting temperature is $kT_{\rm s}$= 0.1 keV; and with a power-law model for the soft component instead, we have $\Gamma_{\rm s}$= 2.6. For both cases, the best-fitting value of the hard component and the χ^2_ν change little. Using only one power-law model for each component, we have $\Gamma_{\rm h}$= 1.41, $A_{\rm h}$=9.3, $\Gamma_{\rm s}$=4.37, $A_{\rm s}$=1.4 and χ^2_ν=1.67.

Spectral fitting results from the ASCA data and the ASCA/ROSAT data are listed in Table 3b. Fig. 4 shows the folded spectra of the ASCA and the ROSAT data as well as the best-fit MODEL A and its components.

3.4.2 Two Power-law Model of the Extragalactic XRB

As ROSAT data have resolved a certain fraction of the XRB below SIS limits into very soft sources, the extragalactic XRB is probably composed of two power-law components. Thus we fit the combined 0.5–2 keV PSPC data and 0.5–7 keV SIS data jointly by a three-component model including one thermal and two power-law models to take contributions from the Galactic halo, AGN-like sources and the yet-unknown XRB sources into account (MODEL B). With the photon index of the AGN spectrum $\Gamma_{\rm src}$ fixed at 2.5, we have obtained the best-fitting $A_{\rm src} = 3.16$, $\Gamma_{\rm XRB} = 1.37$ and $A_{\rm XRB} = 8.28$ (χ^2_ν=1.46). The unfolded data and models are

Table 3 (b). Best-fitting parameters of various XRB spectrum models

MODEL	Γ_s	A_s	kT_s	Γ_h	A_h	kT_h	χ^2_ν
ASCA SIS							
P (1–7 keV)	–	–	–	$1.44^{+0.08}_{-0.07}$	10.10 ± 0.60	–	1.15
P (1–3 keV)	–	–	–	1.33 ± 0.13	9.70 ± 0.70	–	1.01
P (3–7 keV)	–	–	–	$1.36^{+0.44}_{-0.41}$	$8.50^{+6.80}_{-3.80}$	–	1.34
W (P + R)	–	–	–	$1.44^{+0.07}_{-0.06}$	10.20 ± 0.50	0.12	1.24
W (P_h + R) + P_s	0.36	0	–	1.44	10.2	0.12	1.26
W (P + R_h) + B	–	–	0.10	1.44	10.2	0.12	1.25
W (P_h) + P_s	$4.33^{+1.29}_{-0.94}$	$1.36^{+1.64}_{-0.86}$	–	$1.41^{+0.11}_{-0.14}$	$9.60^{+1.10}_{-1.60}$	–	1.70
MODEL A							
W (P + R_h) + R_s	–	–	0.04	1.44	10.2	0.11	1.25
ASCA+ROSAT							
P (1–7 keV)	–	–	–	$1.48^{+0.06}_{-0.09}$	10.3/10.8	–	1.15
P (1–3 keV)	–	–	–	1.44 ± 0.11	10.3/10.8	–	1.15
W (P_h + R) + P_s	$4.84^{+0.90}_{-0.70}$	$0.07^{+0.23}_{-0.00}$	–	1.45 ± 0.06	$10.40^{+0.40}_{-0.30}$	0.12	1.163
W (P + R_h) + B	–	–	0.1	$1.42^{+0.06}_{-0.05}$	$10.20^{+0.40}_{-0.30}$	0.14	1.13
W (P_h) + P_s	4.37	1.4/1.04	–	1.41	8.8/9.5	–	1.665
MODEL A							
W (P + R_h) + R_s	–	–	0.05	$1.46^{+0.05}_{-0.06}$	10.50 ± 0.30	0.12	1.12
MODEL B	Γ_{src} (fixed)	A_{src}		Γ_{XRB}	A_{XRB}	kT_h	χ^2_ν
(above 0.5 keV)							
W (P_{XRB} + P_{src} + R_h)	2.5	3.2		1.37	8.3	0.09	1.46
	3.0	1.8		1.44	9.6	0.09	1.46

1 Codes of the model:
P–power-law,
R–Raymond-smith hot plasma, with redshift=0 and abundance=1 fixed
W–Galactic HI absorption, fixed at 1.66×10^{20} cm^{-2}
B–thermal bremsstrahlung model.
2 Symbols of the model component (subscript s/h indicates the soft/hard component):
Γ–photon index of the power-law component,
A–normalization of the power-law component in keV cm^{-2} s^{-1} sr^{-1} keV^{-1},
kT–temperature of the thermal model (either Raymond-smith or bremsstrahlung) in keV.
"–"– component not involved.
3 The boundary of the soft/hard band in this model fitting is around 0.5 keV where the significance of the Galactic absorption changes.

shown in Fig. 5. The confidence intervals of Γ_{XRB} and A_{XRB} are represented by the large contours in Fig. 6, in which the small contours are the confidence intervals when one more constraint of $A_{src} = 3.16$ is applied. We will use these results to constrain the AGN contribution to the XRB in the next section.

4. DISCUSSION

4.1 The XRB dilemma: very soft resolved sources and hard spectrum

Previous ROSAT observations (eg Shanks et al 1991; Hasinger et al 1993) have shown that up to 70 per cent of the observed XRB (as seen by the *Einstein* Observatory) could be resolved by ROSAT and most of the resolved point sources have been identified as AGN. However, according to our spectral analysis of the XRB and the resolved sources, the contributions from sources like AGN are probably less significant than previously indicated and are mainly in the soft band where the extragalactic and the Galactic components are not easily distinguished. To compensate for the spatially-resolved sources in the soft image and the flat XRB spectrum in the hard band, the Galactic contribution must become smaller. In the following subsections, we will use the spectral fitting results and observed log$N$-log$S$ to constrain the AGN contribution to the broad band XRB and some spectral properties of the unresolved XRB sources.

4.2 Spectral constraints on the AGN contribution to the XRB

Using the results of our ASCA/ROSAT joint fit called MODEL B, we can estimate the ratio of the AGN contribution to the XRB= $I_{src}/(I_{src} + I_{XRB})$. As already shown in the last section, the best fits of ASCA/ROSAT data above 0.5 keV from MODEL B are $\Gamma_{XRB} = 1.37$, $A_{XRB} = 8.28$ and $A_{src} = 3.16$ when Γ_{src} is fixed at 2.5; therefore, the ratio is

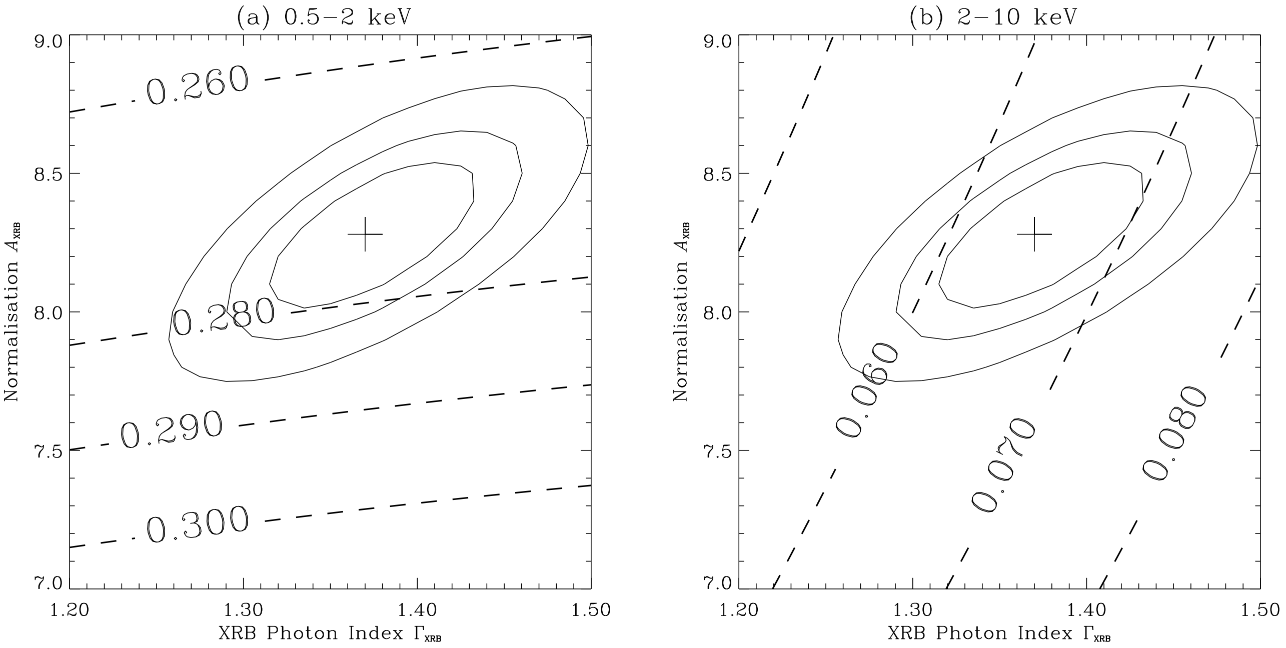

Figure. 7 The ratio of the AGN contribution to the XRB. The solid contour lines are the same as the small contours in Fig. 6. With $\Gamma_{\rm src}$ and $A_{\rm src}$ fixed, the ratio of $I_{\rm src}/(I_{\rm src}+I_{\rm XRB})$ is calculated over the $\Gamma_{\rm XRB}$, $A_{\rm XRB}$ space, which is represented by the dashed contours. (a) Ratio calculated in the 0.5–2 keV band (b) in the 2–10 keV band.

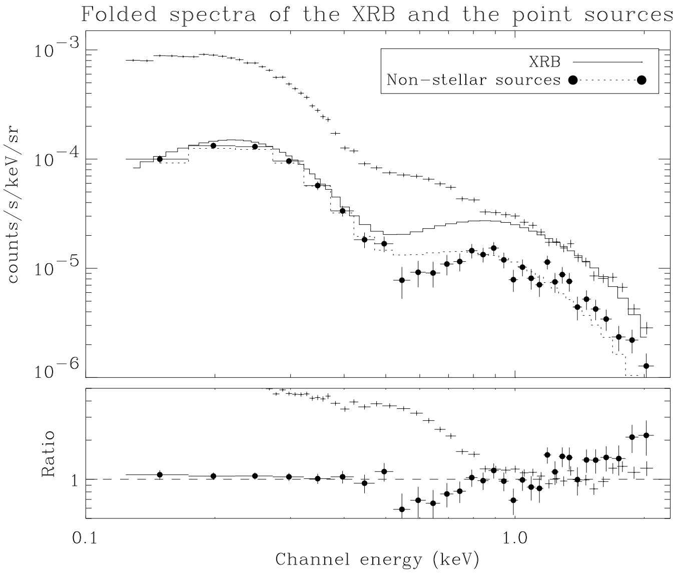

Figure. 8 The folded spectrum of the XRB and the accumulated non-stellar spectrum RS_QA (the filled circles) from the same ROSAT data. The dotted line is the best-fitting power-law model of the non-stellar spectrum and the solid line is the power-law component of the best-fitting XRB model (the best-fit of $\alpha = 1$ in Table 4). The deviation of the folded XRB spectrum to the solid line shows a large soft excess of the XRB below 1 keV. The ratio of the data to the power-law component is shown in the bottom panel.

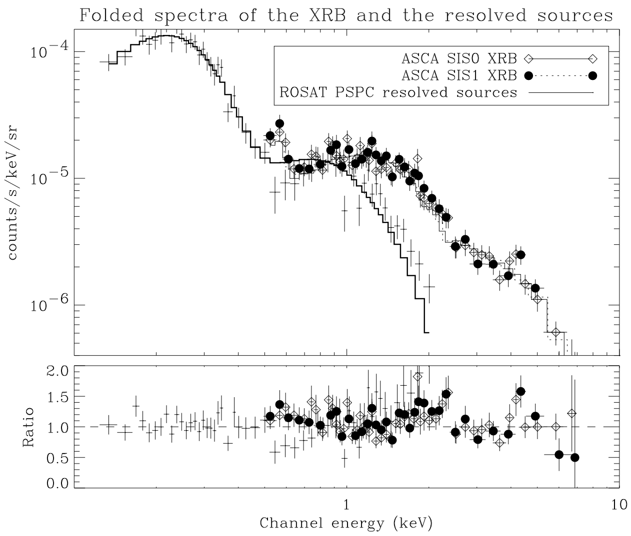

Figure. 9 Folded spectra of the SIS XRB (0.4–7 keV) and the PSPC non-stellar point sources RS_QA (0.1–2 keV).

27.4, 6.5 and 12.7 per cent in the 0.5–2 keV, 2–10 keV and 0.5–10 keV band. Holding the steep power-law spectrum fixed, we can calculate the ratio over the $\Gamma_{\rm XRB}$, $A_{\rm XRB}$ space covering their 3σ confidence intervals as show in Figs. 7a and 7b for the soft and hard band, respectively. As indicated by the dashed contour lines, which represent the ratio, the 3σ AGN contribution to the soft XRB is well below 33 per cent, and the hard XRB below 10 per cent.

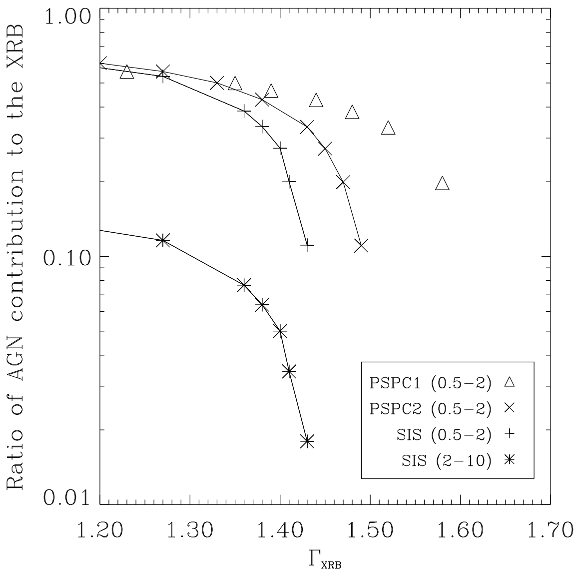

Figure. 10 The variation of $\Gamma_{\rm XRB}$ of the soft-AGN-free XRB spectrum with the fractional contribution of the soft AGN, based on Tables 4–6. PSPC1 refers to the fitting results of the PSPC soft-AGN-free XRB and PSPC AGN RS_QA spectra shown in Table 4 and PSPC2 is obtained from the fitting of the PSPC XRB (with the three brightest sources excised only) and PSPC AGN RS_QA spectra in Table 5. SIS (0.5–2 keV) is the result shown in Table 6, using the PSPC XRB and PSPC AGN spectra, while SIS (2–10 keV) is derived from SIS (0.5–2 keV) data according to the power-law model of the XRB.

A direct comparison of the XRB with faint extragalactic source spectra is shown in Fig. 8, where we use RS_QA and the soft-AGN-free XRB spectrum observed with ROSAT. The XRB spectrum is fit by MODEL A with temperatures of both the soft and hard thermal components fixed to the best-fitting values from the ASCA/ROSAT joint fitting. Without constraining the hard band data, the power-law component of the XRB has $\Gamma = 1.63^{+0.17}_{-0.15}$ and normalization $A = 6.90^{+0.30}_{-0.30}$ keV cm^{-2} s^{-1} sr^{-1} keV^{-1}, whereas the point source has $\Gamma = 2.76^{+0.07}_{-0.06}$ and $A = 3.09^{+4.07}_{3.51}$ (the area is scaled according to the XRB data). In Fig. 8 only the power-law components are shown, where we can see the XRB power-law (the solid line) is harder than the non-stellar spectrum RS_QA (the dotted line). Below 1 keV, the XRB has a large soft excess of possible Galactic origin.

If sources fainter than the threshold have the same spectral shape as brighter ones, then we can measure a soft-AGN-free XRB spectrum by defining the extragalactic component of the XRB

$$I_{\rm tot} = I_{\rm XRB} + I_{\rm src} = \int A_{\rm XRB} E^{-\gamma_{\rm XRB}} + \alpha \int A_{\rm src} E^{-\gamma_{\rm src}}, \quad (1)$$

where $A_{\rm XRB}E^{-\gamma_{\rm XRB}}$ is the soft-AGN-free XRB spectrum and $A_{\rm src}E^{-\gamma_{\rm src}}$ is the best-fitting effective spectrum of the underlying unresolved point sources and its contribution to the XRB is scaled by a factor α. Varying the value of α, we have obtained several sets of $A_{\rm XRB}$, $\gamma_{\rm XRB}$, $A_{\rm src}$, $\gamma_{\rm src}$ and the amplitudes of the two component thermal emission, $A_{T_{\rm h}}$, $A_{T_{\rm s}}$ (Table 4). From Columns 1–5 in Table 4, the ratio of $I_{\rm src}/I_{\rm tot}$ can be calculated, where $I_{\rm tot}$ and $I_{\rm src}$ are defined

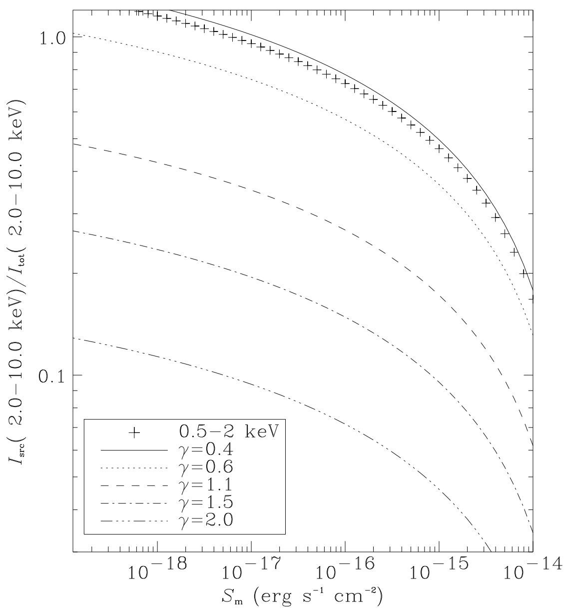

Figure. 11 The contribution of discrete sources to the XRB. The ratio is $I_{\rm src}(E_{\rm L} - E_{\rm H})/I_{\rm tot}(E_{\rm L} - E_{\rm H})$ according to the observed log$N$-log$S$ (Hasinger et al 1993) and the XRB spectrum (this work). The crosses represent the ratio of $(E_{\rm L}, E_{\rm H}) = (0.5, 2)$ keV which is $\gamma_{\rm src}$-independent, the other lines are ratios of different $\gamma_{\rm src}$ ($\gamma_{\rm src}$=$\Gamma_{\rm src} - 1$) in the 2–10 keV band as indicated in the legend. Note $S_{\rm m}$ is always in the 0.5–2 keV band.

as Eq. (1). We plot this result against $\Gamma_{\rm XRB}$ in Fig. 10 (the triangles). Replacing the background data by the ASCA (Fig. 9) and ROSAT data used in Sec. 3 separately (which have more brighter sources), we repeat the same steps and fitting (Tables 5–6). In Fig. 10, the crosses and asterisks are, respectively, ratios in 0.5–2 keV and 2–10 keV based on results of the SIS XRB/PSPC AGN fitting (Table 6). If $\Gamma_{\rm XRB}$ is constrained between 1.4 and 1.5, then the soft-AGN contribution is less than 30 and a few per cent in 0.5–2 keV and 2–10 keV, respectively.

4.3 log$N$-log$S$ constraints on the AGN contribution to the XRB

Another approach to estimating the contribution from discrete sources to the XRB involves the observed log$N$-log$S$ of the resolved sources. Measurements of the log$N$-log$S$ in the soft X-ray band have been derived by using ROSAT data [Hasinger et al , 1993 and Barcons et al , 1994 (in 0.5–2 keV and 0.9–2.4 keV, respectively)] and in the 2–10 keV band by using HEAO-1 A2 and *Ginga* data (Butcher et al 1995). Here we use the result from Hasinger et al (1993) to calculate the total emission from the point source in the $E_{\rm L}$–$E_{\rm H}$ band,

$$I_{\rm src}(E_{\rm L} - E_{\rm H}) = \int_{S_{\rm m}}^{S_{\rm t}} SN(S)\, dS \frac{\int_{E_{\rm L}}^{E_{\rm H}} E^{-\gamma_{\rm src}}\, dE}{\int_{0.5}^{2} E^{-\gamma_{\rm src}}\, dE}, \quad (2)$$

where $N(S)$ is the differential number density of sources at the flux S, $S_{\rm t}$ is the flux threshold beyond which sources cannot be detected and $S_{\rm m}$ is the faint end where point sources cease their contribution to the XRB (or otherwise

Table 4. Best fit of the PSPC soft-AGN-free XRB and PSPC AGN RS_QA spectra

α	$\Gamma_{\rm src}$	$A_{\rm src}$	$\Gamma_{\rm XRB}$	$A_{\rm XRB}$	$A_{T_{\rm h}}$	$A_{T_{\rm s}}$	χ^2_ν
0	2.76	3.09	1.63	6.88	34.17	8.26	1.063
0.2	2.76	3.10	1.58	6.31	33.14	8.18	1.071
0.4	2.75	3.11	1.52	5.74	32.09	8.11	1.083
0.5	2.75	3.11	1.48	5.45	31.56	8.07	1.090
0.6	2.75	3.12	1.44	5.16	31.02	8.04	1.098
0.7	2.74	3.13	1.39	4.88	30.47	8.00	1.106
0.8	2.74	3.13	1.35	4.59	29.92	7.96	1.114
1	2.73	3.15	1.23	4.00	28.80	7.90	1.132
2	2.66	3.34	−1.66	0.56	22.49	7.62	1.229
4	2.91	2.07	−3.00	0.19	10.31	6.94	1.860

*The degree of freedom is 331 for all the fittings.

Table 5. Best fit of the PSPC XRB and PSPC AGN RS_QA spectra

α	$\Gamma_{\rm src}$	$A_{\rm src}$	$\Gamma_{\rm XRB}$	$A_{\rm XRB}$	$A_{T_{\rm h}}$	$A_{T_{\rm s}}$	χ^2_ν
0	2.76	3.09	1.51	10.94	51.49	11.55	1.064
0.1	2.76	3.09	1.49	10.66	50.95	11.52	1.068
0.2	2.76	3.10	1.47	10.38	50.41	11.48	1.071
0.3	2.76	3.10	1.45	10.10	49.86	11.44	1.075
0.4	2.75	3.10	1.43	9.81	49.32	11.40	1.079
0.6	2.75	3.11	1.38	9.24	48.20	11.32	1.088
0.8	2.75	3.12	1.33	8.66	47.08	11.25	1.099
1.0	2.74	3.13	1.27	8.08	45.95	11.17	1.110
1.2	2.73	3.14	1.20	7.50	44.80	11.10	1.122
1.4	2.73	3.15	1.12	6.90	43.65	11.03	1.135
1.6	2.72	3.17	1.03	6.30	42.50	10.96	1.149
2.0	2.71	3.20	0.79	5.05	40.14	10.83	1.180
4.0	2.72	2.93	−3.00	0.45	26.48	10.42	1.353

*The degree of freedom is 334 for all the fittings.

Table 6. Best fit of the PSPC AGN RS_QA spectrum and the SIS XRB spectrum

α	$\Gamma_{\rm src}$	$A_{\rm src}$	$\Gamma_{\rm XRB}$	$A_{\rm XRB}$	$A_{T_{\rm h}}$	$A_{T_{\rm s}}$	χ^2_ν
0	2.76	3.09	1.45	10.26	24.77	242.73	1.081
0.1	2.76	3.09	1.43	9.98	24.20	287.04	1.080
0.2	2.76	3.09	1.41	9.70	23.64	324.67	1.082
0.3	2.76	3.08	1.40	9.42	23.14	350.77	1.084
0.4	2.76	3.08	1.38	9.15	22.46	417.56	1.087
0.5	2.76	3.08	1.36	8.88	21.58	524.6	1.090
0.9	2.76	3.07	1.27	7.80	19.10	688.03	1.106
2	2.77	2.98	1.01	5.20	9.20	1702.02	1.188

*The degree of freedom is 307 for all the fittings.

over-produce the XRB). With the XRB spectrum obtained from the last section, we plot the ratio of the soft-AGN contribution to the XRB $I_{\rm src}(E_{\rm L}-E_{\rm H})/I_{\rm XRB}(E_{\rm L}-E_{\rm H})$ as a function of $S_{\rm m}$ in 0.5–2 keV and 2–10 keV in Fig. 11, for $\Gamma_{\rm src}$ varying from 1.4 to 3, where $I_{\rm XRB}$ is obtained from the results of MODEL A in Table 3b. As shown in Fig. 11, the soft XRB in 0.5–2 keV is likely saturated by AGN when $S_{\rm m}$ is about 10^{-17} erg cm^{-2} s^{-1}; however, in the 2–10 keV band—as we have to extrapolate the log$N$-log$S$ measurement to this band—the results are diverse and highly depend on the spectral shape of the faint sources. As shown in previous subsections, the contribution from soft AGN to the 2–10 keV XRB is at most 10 per cent; therefore, the faint end of AGN is at $\sim$ a few times 10^{-14} to 10^{-16} erg cm^{-2} s^{-1}.

5. CONCLUSION

Having analysed data observed with ASCA and ROSAT and from our results shown in Table 3b, we find that the energy distribution of the extragalactic XRB in 1–7 keV is indeed consistently flat, and it is well fit by a single power-law model with photon index from 1.4 to 1.5. The softer best-fitting results from previous ROSAT data fitting is probably due to less independent channel bins and constraints to confine the complicated XRB model. Actually with a relatively larger error bar, some earlier ROSAT observations of the XRB did not rule out a flat soft XRB (eg Fig. 3a in Chen et al 1994). Now the joint fit with the ASCA in this work has provided more constraints on the model fitting and improved the confinement of best-fitting values.

The spectral fitting result of the XRB alone is in agreement with the previous work using ASCA (Gendreau et al 1995 and see the introduction) and recent work with the ROSAT data (Chen et al 1994; Georgantopoulos et al 1996). Most importantly, our work uses high quality data to integrate the observations across the 0.1–3 keV band and the 3–7 keV band and provides some more evidence for the single power-law model of the XRB spectrum in this bandpass.

This result supports the idea that the origin of the XRB below and above 3 keV could be the same class of sources plus partial contributions from AGN. AGN may have less contributions to the XRB than previous estimates; moreover, our analysis has shown resolved source spectra in this field have a softer spectrum than that of the average AGN. The soft sources—similar to but fainter than the resolved ones—probably contribute only 30 per cent below 2 keV and less than 10 per cent above it. Since the energy density of the X-ray sky increases from 0.1 keV onwards, the main contributor to the XRB lies in the hard band. These spectrally different population is expected to be further identified in future X-ray deep surveys.

ACKNOWLEDGMENTS

CLW thanks members in the Cambridge X-ray Astronomy group and Ascahelp on-line at GSFC for various technical advice. The ROSAT data were downloaded from the UK ROSAT Archive Centre at Leicester.

REFERENCES

Boldt E., 1987, Phys. Rep., **146**, 215
Boyle B. J., Fong R, Shanks T., Peterson B. A., 1990, MNRAS, **243**, 1
Butcher J. A. et al , 1995, MNRAS, in press
Chen L.-W., Fabian A. C., Warwick R. S., Branduardi-Raymont G., Barber C. R., 1994, MNRAS, **266**, 846
Day C., Arnaud K. A., Ebisawa K., Gotthelf E., Ingham J., Mukai K., White N., 1994, The ABC Guide to ASCA Data Reduction version 4, ASCA Guest Observer Facility, NASA (The ABC Guide)
Gendreau K., 1995, Ph.D. thesis, Massachusetts Institute of Technology.
Gendreau K. et al , 1995, PASJ, **47**, L5
Fabian A. C., Barcons X., 1992, ARA & A, **30**, 429
Fabian A. C., et al , 1994, in Makino F., Ohashi T., eds, The New Horizon of X-ray Astronomy. University Academy

Press Inc, Tokyo
Georgantopoulos I., Stewart G. C., Shanks T., Boyle B. J., Griffiths R. E., 1996, MNRAS, **280**, 276
Hasinger G., et al , MPE/OGIP Calibration Memo CAL/ROS/93-015, 1995 May 08 Version.
Hasinger G., 1992, in Barcons X., Fabian A. C., eds, The X-ray Background, Cambridge Univ. Press, Cambridge, p. 229
Hasinger G., Burg R., Giacconi R., Hartner G., Schmidt M., Trümper J., Zamorani G., 1993, A & A, **275**, 1
Heiles H., Cleary M. N., 1979, AJPAS, **47**, 1
McCammon D., Sanders W. T., 1990, ARA & A, **28**, 657
Madau P., Ghisellini G., Fabian A. C., 1994, MNRAS, **270**, L17
Marshall F., Bold E. A., Holt S. S., Miller R. B., Mushotzky R. F., Rose L. A., Rothschild R. E., Serlemitsos P. J., 1980, ApJ, **235**, 4
Nandra K., 1991, Ph.D. thesis, Univ. Leicester
Plucinsky P. P., Snowden S. L., Briel U. G., Hasinger G., Pfeffermann E., 1993, ApJ, **418**, 519
Schartel N., Walter R., Fink H. H, 1994, in Courvoisier T. J.-L., Belcha A., Multi-Wavelength Continuum emission of AGN, Kluwer Academic Publishers, Dordrecht, p. 373
Serlemitsos P. J., Jalota L., Soong Y., Awaki H., Itoh M., Ogasaka Y., Honda H., Uchibori Y., PASJ, **47**, 105
Shanks T., Georgantopoulos I., Stewart G. C., Pounds K. A., Boyle B. J., Griffiths R. E., 1991, Nature, **353**, 315
Snowden S. L., McCammon D., Burrows D. N., Mendenhall J. A., ApJ, 1994, **424**, 714
Tanaka Y., Inoue H., Holt S., 1994, PASJ, **46**, L37
Turner T. J., Pounds K. A., 1989, MNRAS, **240**, 833
Wang Q. D., McCray R., 1993, ApJ, **409**, L37
Williams O. R., Turner M. J. L., Stewart G. C., Saxton R. D., Ohashi T., et al , 1992, ApJ, **389**, 157
Wu X., Hamilton T., Helfand D. J., 1991, ApJ, **379**, 564

This paper has been produced using the Blackwell Scientific Publications TEX macros.